remote sensing

MDPI

Article

Seabed Depth Prediction Using Multi-Scale Gravity Anomalies and Fully Connected Deep Neural Networks: A Novel Approach Applied to the South China Sea

Jiajia Yuan [1,2,*], Chen Yang [1], Di Dong [2], Jinyun Guo [3], Dechao An [4] and Daocheng Yu [5]

[1] School of Geomatics, Anhui University of Science and Technology, Huainan 232001, China; 2023201543@aust.edu.cn
[2] Key Laboratory of Marine Environmental Survey Technology and Application, Ministry of Natural Resources, P.R. China, Guangzhou 510300, China; dongdide90@163.com
[3] College of Geodesy and Geomatics, Shandong University of Science and Technology, Qingdao 266590, China; guojy@sdust.edu.cn
[4] School of Geospatial Engineering and Science, Sun Yat-sen University, Zhuhai 519082, China; andch@mail2.sysu.edu.cn
[5] School of Geomatics, Liaoning Technical University, Fuxin 123000, China; yudaocheng@lntu.edu.cn
* Correspondence: yuanjiajia@aust.edu.cn

Abstract: Accurate seabed topography is crucial for marine research, resource exploration, and engineering applications. While deep learning techniques have been widely applied in seabed inversion, existing methods often overlook the multi-scale influence of gravity anomalies, particularly the critical role of short-wavelength gravity anomalies in resolving fine-scale bathymetric features. In this study, we propose a novel Fully Connected Deep Neural Network (FCDNN) approach that systematically integrates long-wavelength, short-wavelength, and residual gravity anomaly components for seabed topography inversion. Using multi-satellite altimetry-derived gravity anomaly data (SIO V32.1) and shipborne bathymetric data (NCEI), we constructed a high-resolution ($1' \times 1'$) seabed topography model for the South China Sea (108°E–121°E, 6°N–23°N), termed FCD_Depth_SCS. The workflow included multi-scale decomposition of gravity anomalies, linear regression-based residual calculation, and FCDNN-based nonlinear training to capture the complex relationships between gravity anomalies and water depth. The FCD_Depth_SCS model achieved a difference standard deviation (STD) of 44.755 m and a mean absolute percentage error (MAPE) of 2.903% when validated against 160,476 shipborne control points. This performance significantly outperformed existing models, including GEBCO_2024, SIOv25.1, DTU18, and GGM_Depth (derived from the Gravity–Geologic Method), whose STDs were 82.234 m, 108.241 m, 186.967 m, and 58.874 m, respectively. Notably, the inclusion of short-wavelength gravity anomalies enabled the model to capture fine-scale bathymetric variations, particularly in open-sea regions. However, challenges remain near coastlines and complex terrains, highlighting the need for further model partitioning to address localized nonlinearity. This study highlights the benefits of integrating multi-scale gravity anomaly data with a fully connected deep neural network. Employing this innovative and robust approach enables high-resolution inversion of seabed topography with enhanced precision. The proposed method provides significant advancements in accuracy and resolution, contributing valuable insights for marine environmental research, resource management, and oceanographic studies.

Keywords: fully connected deep neural network; seabed topography; gravity anomaly; satellite altimetry

check for updates

Academic Editor: Andrzej Stateczny

Received: 22 December 2024
Revised: 15 January 2025
Accepted: 24 January 2025
Published: 25 January 2025

Citation: Yuan, J.; Yang, C.; Dong, D.; Guo, J.; An, D.; Yu, D. Seabed Depth Prediction Using Multi-Scale Gravity Anomalies and Fully Connected Deep Neural Networks: A Novel Approach Applied to the South China Sea. *Remote Sens.* **2025**, *17*, 412. https://doi.org/10.3390/rs17030412

Copyright: © 2025 by the authors. Licensee MDPI, Basel, Switzerland. This article is an open access article distributed under the terms and conditions of the Creative Commons Attribution (CC BY) license (https://creativecommons.org/licenses/by/4.0/).

1. Introduction

The ocean is a vital resource for sustainable human development, and its rational exploration and utilization depend on accurate seabed topography information. Such information is essential for the planning and execution of marine development strategies [1]. Seabed surveys are essential for marine mapping. Traditionally, they use ships with positioning systems and sonar to measure depths and detect obstacles. However, deep-sea survey efforts are predominantly focused on areas such as ocean ridges, resulting in uneven bathymetric data coverage. Large gaps in data persist across vast ocean regions due to factors such as ship speed, navigation routes, and natural conditions. These limitations hinder our comprehensive understanding of seabed geomorphology, constraining advancements in scientific research, resource development, and ecological conservation [2–5].

Satellite altimetry technology has introduced innovative approaches to seabed topography mapping, offering all-weather, continuous operational capabilities, extensive global coverage, and rapid data acquisition [6]. Consequently, ocean gravity anomaly data derived from altimetry can be used to invert seafloor topography, offering essential data support for scientific research on Earth system processes [7,8].

Several commonly used methods for seafloor topography inversion based on gravity anomaly data include the Gravity–Geologic Method (GGM) [9,10] and its improved variants [11], the admittance function method [12], the Smith and Sandwell method (S&S) [13], and the least squares method [14]. While these methods provide relatively reliable models of seafloor topography, they each have notable limitations. For instance, although the GGM and its improved versions achieve high accuracy, they require extensive control point data, overlook the nonlinear relationship between gravity anomalies and water depth, and exhibit poor inversion accuracy in shallow water areas. The admittance function method, which uses the correlation between gravity anomalies and water depth to transform the model in the frequency domain, is well-suited for regions lacking ship survey data. However, its spatial resolution is low [15]. The S&S method leverages shipborne bathymetric data as prior information, which aids in resolving geophysical parameter selection challenges. Nonetheless, its single-point fitting approach is highly sensitive to complex measurement conditions and geological variations, potentially leading to extreme value errors [16]. Furthermore, these methods typically emphasize the linear relationship between ocean gravity data and seafloor topography, failing to fully account for nonlinear factors [17]. Although the nonlinear iterative least squares method addresses some of these limitations, it remains inefficient in terms of computational speed and processing time. Consequently, there is an urgent need to explore and develop more efficient algorithms to enhance modeling efficiency and inversion accuracy [14].

The advancement of modern computer technology has significantly enhanced the ability to study complex seabed topography. As a forefront research direction in machine learning, deep learning aims to equip systems with human-like analytical and learning capabilities, enabling them to effectively process and recognize various types of data, including text, images, and sounds. This technology has proven invaluable across numerous fields, offering vast opportunities for scientific research and practical applications [18,19]. In the earth sciences, deep learning is widely applied to earth observation and remote sensing research due to its capacity to model the inherent nonlinear relationships within large-scale datasets flexibly and effectively.

Neural networks are a key representation of deep learning, capable of automatically extracting features from large-scale datasets. This ability significantly enhances prediction accuracy and decision-making processes, making neural networks widely applicable in fields such as object detection, pattern recognition, and image processing. Neural networks, inspired by the interconnected structure of neurons in the human brain, excel at achieving

complex nonlinear mappings. By fine-tuning their weights and parameters, they optimize performance and, in some tasks, can even exceed human capabilities. These advancements have been instrumental in driving the development of artificial intelligence.

The Fully Connected Deep Neural Network (FCDNN) is a fundamental architecture of artificial neural networks, where each neuron is connected to all neurons in the previous layer. This structure enables FCDNNs to capture complex nonlinear relationships, making them well-suited for a wide range of data types and tasks [20].

Neural networks have been extensively applied across various research fields, including geology, meteorology, and automation technology [21–23]. For example, Lumban-Gaol et al. [24] utilized a convolutional neural network (CNN) combined with Sentinel-2 satellite images and LiDAR/multi-beam echo sounder reference data to achieve a depth measurement accuracy of 1.3–1.94 m. This accuracy was significantly enhanced by employing a 9×9 window size and short-wave infrared bands under diverse water conditions. Zhou et al. [25] employed a multi-layer perceptron (MLP) neural network with ocean geodetic data to establish a bathymetric model of the Gulf of Mexico. Yang et al. [20] compared the performance of Fully Connected Deep Neural Networks (FCDNN) and convolutional neural networks for seabed bathymetric prediction, finding that FCDNN outperformed CNNs in predicting wavelengths shorter than 6 km. Zhu et al. [26] proposed a novel approach for inverting high-precision ocean gravity anomalies using multi-channel convolutional neural networks. This method addressed the limitations of traditional approaches, which often neglect nonlinear features, demonstrating its potential in gravity anomaly inversion. Zhou et al. [19] utilized multi-source ocean geodetic data to train a model for predicting water depths in the Caribbean Sea. They validated the reliability and effectiveness of the bathymetry inversion method based on an MLP neural network by comparing its predictions with those of other models. Additionally, Wang et al. [27] applied a CNN-based method to integrate gravity information and shipborne bathymetric data, achieving a significant improvement in model accuracy for seabed topography inversion in the South China Sea. Harper et al. [28] designed and trained a neural network to predict global seafloor topography using gravity anomalies. By employing geographic partitioning to address the issue of independence between training and test datasets, they achieved a root mean square error improvement of 16%, reducing the error from 165 m in the old model to 138 m in the final model. This highlights the versatility and effectiveness of neural networks in advancing seabed topography inversion and related research.

Gravity anomaly data, particularly short-wavelength gravity anomaly data, play a pivotal role in the field of seafloor topography inversion [5,20,29]. While many researchers have acknowledged the impact of short-wavelength gravity anomalies on seabed topography in existing studies, these data have yet to be fully utilized in seafloor topography inversion research. Short-wavelength gravity anomalies are often closely associated with the distribution of subsurface matter, tectonic activity, and crustal deformation [30]. Given the complexity and diversity of seafloor topography, short-wavelength gravity anomaly data can highlight small yet critical topographic features that may be overlooked or inaccurately represented by traditional surveying methods. Therefore, in this study, gravity anomaly data were separated into long- and short-wavelength gravity anomalies, as well as residual long- and short-wavelength gravity anomaly signals, for bathymetric inversion. This approach aims to highlight the advantages of short-wavelength gravity signals in seafloor depth inversion.

In this study, the Fully Connected Deep Neural Network (FCDNN) was employed to integrate shipborne bathymetric data and satellite altimetry gravity anomaly data, including long- and short-wavelength gravity anomalies, as well as residual long- and short-wavelength gravity anomalies. Using this approach, a seabed terrain model for the

South China Sea (108°E–121°E, 6°N–23°N) with a grid resolution of $1' \times 1'$, termed the FCD_Depth_SCS model, was constructed. The inversion results were compared with existing models, including GEBCO_2024, SIOv25.1, DTU18, and the GGM_Depth model derived using the Gravity-Geologic Method (GGM), to evaluate the accuracy of the FCD_Depth_SCS model.

2. Study Area and Data Sources

2.1. Study Area

This research focuses on the South China Sea, spanning a longitude range of 108°E to 121°E and a latitude range of 6°N to 23°N. The South China Sea, a marginal sea of southern China located in the western Pacific Ocean, is the world's third-largest marginal sea. Most of the region comprises deep-sea areas, including part of the continental shelf in the northwest and a gently sloping sea in the northeast. The topography is highly complex, featuring numerous seamounts and notable formations such as the Xisha Islands, Zhongsha Islands, and the waters surrounding Scarborough Shoal [31]. According to the ETOPO1 model, the maximum seafloor depth in this area reaches 5132 m, with an average depth of approximately 1860 m [32].

2.2. Gravity Anomaly Data

The gravity anomaly data utilized in this research is derived from the SIO V32.1 gravity anomaly model, released in 2022 by the Scripps Institution of Oceanography (SIO) at the University of California, San Diego (USA) (https://topex.ucsd.edu/pub/global_grav_1min/ (accessed on 20 January 2025)). This model integrates satellite altimetry data from GeoSat, ERS-1/2, Topex/Poseidon, Jason-1/2, CryoSat-2, and Sentinel-3A/B, with a grid resolution of $1' \times 1'$. Compared to its predecessor, SIO V32.1 employs improved data fusion and processing methods, offering enhanced accuracy and resolution.

The SIO V32.1 model not only advances our understanding of the global gravity field but also provides a robust dataset for seafloor terrain inversion and various geological applications. Figure 1 illustrates the gravity anomaly distribution within the study area.

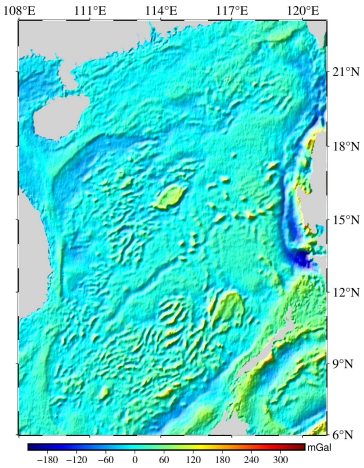


Figure 1. Gravity anomalies in the South China Sea (from the SIOV32.1 model).

2.3. Seabed Topography Model Data

The seabed topography model data used in this study include the GEBCO_2024 model, the SIO 25.1 model, and the DTU18 model. These models are primarily utilized to evaluate the accuracy of the inversion results of this study, with the GEBCO_2024 model additionally employed to correct errors in shipborne bathymetry points.

The GEBCO_2024 model is a global topographic model that integrates terrestrial and seafloor topography measurements and estimations, featuring a grid resolution of 15″. It is based on the SRTM15+ dataset version 2.6, combined with predicted ocean depths and extensive multi-beam data. Using a fusion processor, the model ensures a continuous and high-resolution depiction of submarine topography. The data can be downloaded from https://download.gebco.net/ (accessed on 20 January 2025).

The SIO 25.1 model, released by the Scripps Institution of Oceanography (SIO) in January 2023, is a global seabed topography model with a grid resolution of $1' \times 1'$. The data can be accessed at https://topex.ucsd.edu/pub/global_grav_1min/ (accessed on 20 January 2025).

The DTU18 model, developed by the Technical University of Denmark, is a global seabed topography model designed to represent the mean sea surface height and mean dynamic topography of the ocean, with a grid resolution of $1' \times 1'$. This model is based on years of satellite altimetry and ocean observation data, incorporating multiple data sources to ensure accuracy and reliability.

2.4. Ship Bathymetry Data

The bathymetric data used in this study were provided by the National Centers for Environmental Information (NCEI) in the United States. These data can be accessed and downloaded from https://www.ncei.noaa.gov/maps/geophysics (accessed on 20 January 2025). Established in 2015 as part of the National Oceanic and Atmospheric Administration (NOAA), NCEI is responsible for the collection, management, and dissemination of environmental and climate data. It offers access to shipborne bathymetric data spanning from the 1950s to the present, supporting a wide range of scientific research and applications.

In the South China Sea, NCEI provides 123 single-beam bathymetric trajectories. Considering the potential outdatedness and uncertainties in positioning and bathymetric accuracy of some shipborne bathymetric data, this study adopts the "3σ" principle [33] for error screening and correction. The GEBCO_2024 model is used as a reference to identify and adjust inaccuracies in the shipborne bathymetric data. The specific method involves interpolating the bathymetric values of the GEBCO_2024 model to the locations of the shipborne bathymetric points and calculating the differences between the interpolated values and the ship-measured bathymetry. From these differences, the mean error is determined, and bathymetric points with differences exceeding three times the mean error are excluded as outliers. Because of this screening process, 8653 bathymetric points were eliminated, retaining a total of 802,379 shipborne bathymetric points, with a rejection rate of approximately 1.07%. This ensures a more accurate and reliable dataset for subsequent analysis.

Based on the principle of maintaining a 4:1 ratio between control points and check points [19,34], 641,903 shipborne bathymetry points were randomly selected as control points, while the remaining 160,476 points were designated as check points. Figure 2 illustrates the spatial distribution of the shipborne bathymetry points within the study area. In the figure, the background water depth is represented by the SIOv25.1 model, with white points indicating control points and red points indicating check points. Control points were exclusively used to train the neural network models, while check points were utilized to evaluate the accuracy of the FCD_Depth_SCS model.

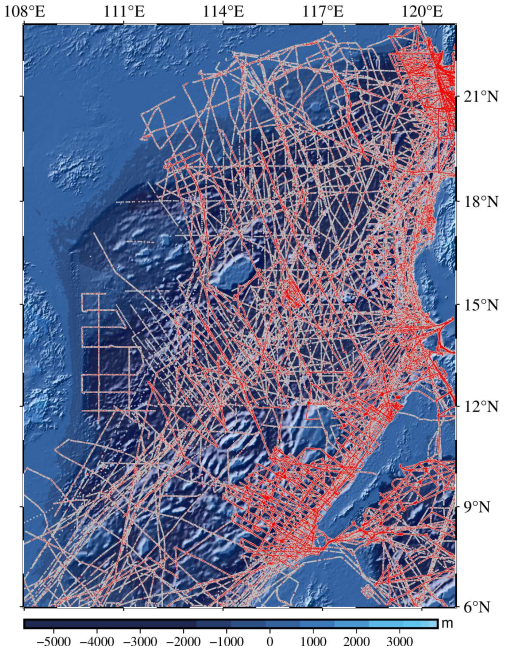


Figure 2. Spatial distribution of shipborne bathymetric trajectories within the study area, where white points represent control points and red points denote check points. The background water depth is derived from the SIO 25.1 model.

3. Methodology

This section focuses on the data processing methods and modeling workflow used to construct a high-resolution submarine topography model. It describes the decomposition of gravity anomalies into long- and short-wavelength components, the calculation of residuals, and the preparation of input features for the neural network. The application of the FCDNN is then detailed, including its architecture, training process, and parameter optimization. Finally, the workflow for constructing the seabed topography model of the South China Sea (FCD_Depth_SCS) is presented, outlining the steps from feature generation to model prediction.

3.1. Long- and Short-Wavelength Gravity Anomalies and Their Residuals

The short-wavelength gravity anomaly primarily reflects subtle variations in local bedrock topography, while the long-wavelength gravity anomaly corresponds to deeper changes in the mass distribution within the Earth's crust [35]. To calculate the short-wavelength gravity anomaly at control points, the Bouguer plate formula is applied, as shown below:

$$\Delta g_{short}(j) = 2\pi G \Delta\rho (E(j) - D) \quad (1)$$

where $\Delta g_{short}(j)$ represents the short-wavelength gravity anomaly at control point j; G is the gravitational constant; $\Delta\rho$ is the constant density; $E(j)$ denotes the sea depth at control point j; and D is the reference sea depth, set as the maximum water depth in the study area, which is -5132 m.

After calculating the short-wavelength gravity anomaly at the control points using Equation (1), the long-wavelength gravity anomaly at the control points is obtained by subtracting the calculated short-wavelength gravity anomaly from the total gravity anomaly (that is the SIO V32.1 gravity anomaly) at the same points. A long-wavelength gravity anomaly field is then constructed based on the long-wavelength gravity anomalies of the control points. Through interpolation, the long-wavelength gravity anomalies at unknown

points are determined, allowing the short-wavelength gravity anomalies at these points to be subsequently calculated.

A linear regression model was applied to establish the linear relationship between long- and short-wavelength gravity anomalies and the shipborne bathymetry values, respectively. Residual gravity anomalies were extracted from the remaining signals to minimize the impact of outliers and reduce signal loss. The shipborne bathymetry values were used as the input variables, while the long-wavelength and short-wavelength gravity anomalies served as the target variables. The model parameters, specifically the slope and intercept of the linear equations, were calculated by minimizing the difference between the predicted and actual values in the training data. The fitted slopes were determined to be -0.029 mGal/m and 0.040 mGal/m, respectively. The reference long- and short-wavelength gravity anomalies were computed by multiplying the shipborne bathymetry data by the fitted slopes. These reference values were then subtracted from the original long- and short-wavelength gravity anomalies to obtain the residual long- and short-wavelength gravity anomalies [36].

The final feature dataset, which serves as the input data for the FCDNN in the depth inversion process, comprises short-wavelength gravity anomalies, long-wavelength gravity anomalies, residual short-wavelength gravity anomalies, and residual long-wavelength gravity anomalies. This dataset encapsulates the key gravity anomaly components and their residuals, which are critical for capturing the nonlinear relationships between gravity signals and bathymetry during the neural network training and inversion stages.

3.2. FCDNN Neural Network Method

The FCDNN is a feedforward neural network known for its exceptional performance in data fitting and feature extraction. Its strong nonlinear modeling capabilities allow it to effectively handle complex nonlinear mappings [20]. This architecture is optimized to adapt quickly and capture intricate data patterns, making it highly suitable for classification and regression tasks across various real-world applications.

For the input vector $x \in R^n$, the fully connected layer first performs a linear transformation:

$$z = Wx + b \tag{2}$$

where $W \in R^{m \times n}$ is the weight matrix, $b \in R^m$ is the bias vector, and $z \in R^m$ is the result of a linear transformation. The results of the linear transformation are nonlinearly mapped through the activation function ReLU:

$$a = f(z) \tag{3}$$

where $a \in R^m$ is the output of this layer. The activated output a is taken as the input to the next layer, and the above steps are repeated until the output layer is reached. In this study, the mean square error (MSE) was used as a loss function to measure the difference between the model output and the true label. The mean square error loss function is suitable for regression tasks, which can effectively measure the difference between the predicted value and the true value.

During the training process, the FCDNN adjusts its parameters using training samples and their corresponding true values. By employing the backpropagation algorithm, the network optimizes its internal weights and biases to minimize the error between predicted and actual values. This iterative process involves several key steps: the network calculates the loss function to assess prediction accuracy and then updates the weights based on error feedback. These updates are repeated until a predefined convergence criterion is met, ensuring the model achieves optimal performance.

The FCDNN model features multiple fully connected layers between the input layer and the output layer, providing data fitting and feature extraction capabilities. By training on positional information (latitude and longitude) and gravity anomaly data (including long-wavelength and short-wavelength gravity anomalies, as well as their residuals), the model approximates the nonlinear mapping relationship between the input features (samples) and the target labels (shipborne bathymetry).

The network architecture designed in this study consists of four fully connected hidden layers, as illustrated in Figure 3. These layers are specifically configured to enable the model to capture the complex nonlinear relationship between gravity field data and seafloor topography, thereby achieving accurate bathymetric predictions.

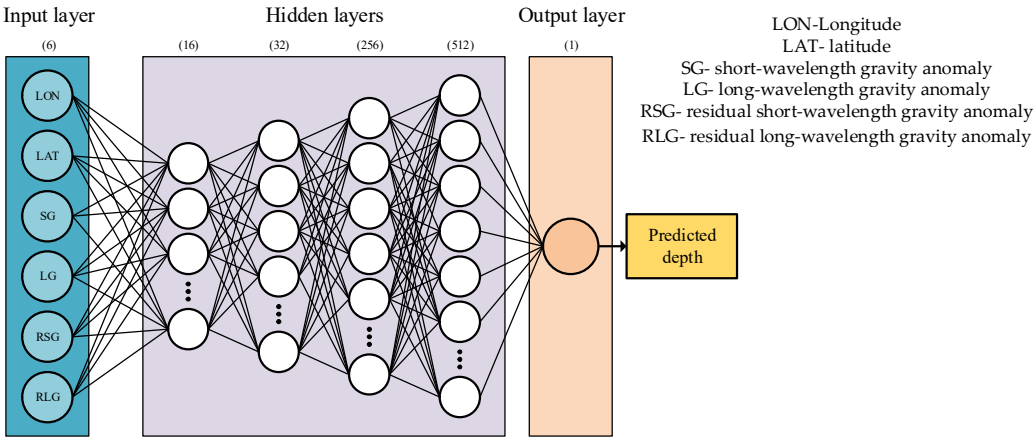


Figure 3. FCDNN neural network structure and input/output data.

Figure 3 illustrates the input data used in this study, which includes longitude (LON), latitude (LAT), short-wavelength gravity anomaly (SG), long-wavelength gravity anomaly (LG), residual short-wavelength gravity anomaly (RSG), and residual long-wavelength gravity anomaly (RLG). To enhance the efficiency of the FCDNN neural network in optimizing weights and biases, the input and output data (data other than longitude and latitude) are standardized as follows:

$$x_{new} = \frac{x - \mu}{\sigma} \tag{4}$$

In the above equation, x_{new} represents the normalized data, x is the data before normalization, μ is the mean of the original data, and σ is the standard deviation of the original data. This normalization process ensures that the dataset has a mean of 0 and a standard deviation of 1, allowing the training data to be scaled uniformly for improved model performance.

3.3. Neural Network Inversion Process

Figure 4 illustrates the process of constructing a seabed topography model. First, following data preprocessing, the shipborne bathymetric data were randomly divided into control point data and checkpoint data in a 4:1 ratio. The control point data were used for model training and parameter estimation, while the checkpoint data were used to evaluate the model's predictive performance. Next, using the control point data, the short-wavelength gravity anomaly was calculated with the Bouguer plate formula, followed by the computation of the long-wavelength gravity anomaly at the control points. Once the short-wavelength and long-wavelength gravity anomaly data were obtained, linear regression was applied separately to the long-wavelength and short-wavelength gravity anomalies to fit the optimal reference values. The residual long-wavelength and short-

wavelength gravity anomalies were then derived by subtracting the fitted reference values from the corresponding gravity anomaly data. The latitude, longitude, and gravity anomaly data of the control points served as input features for training the neural network, while the shipborne bathymetry values were used as output targets. Finally, to accelerate the optimizer's convergence, the input and output data were normalized before being used as the training dataset for the neural network.

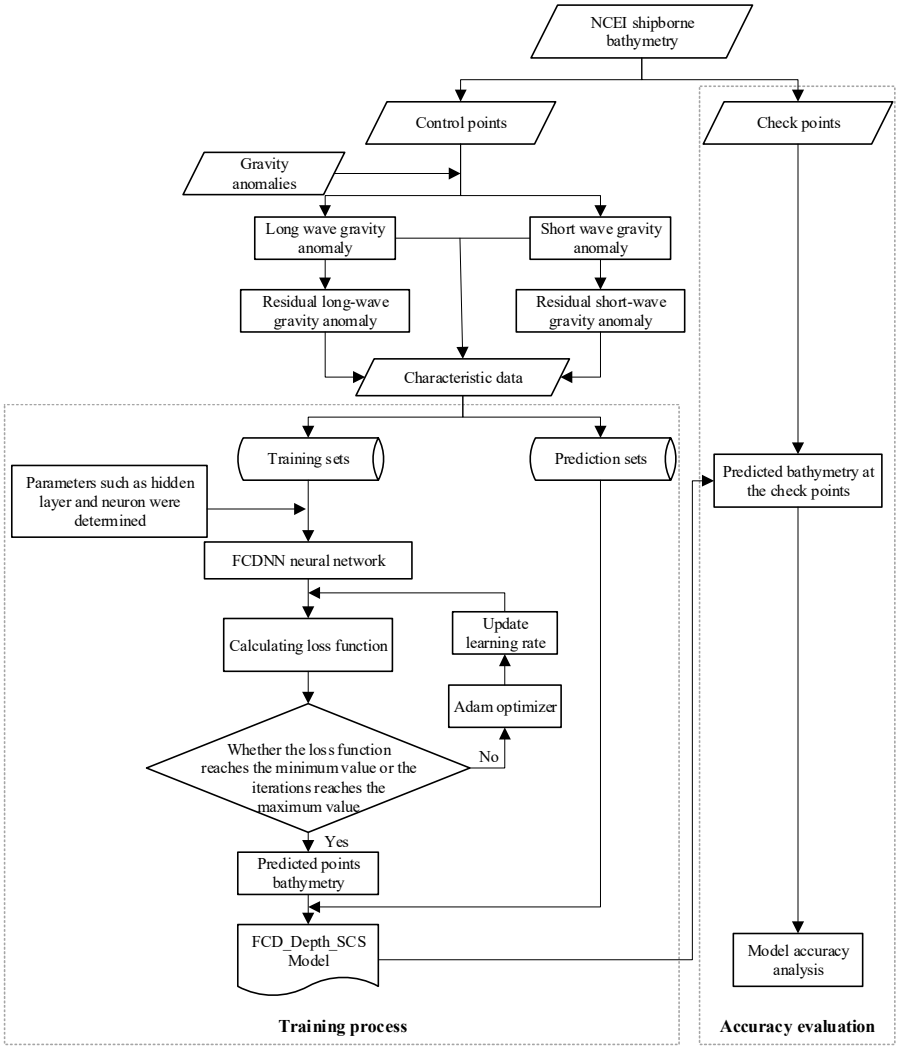


Figure 4. Flowchart of the FCDNN neural network process for submarine topography model inversion.

The neural network is implemented using a Sequential model, where layers are added in order. It consists of four fully connected (Dense) layers with 16, 32, 256, and 512 neurons, respectively, followed by an output layer with a single neuron. This multi-hidden-layer architecture is well-suited for complex tasks, as it enables the network to learn intricate feature representations by hierarchically extracting and constructing higher-level features layer by layer. The number of neurons in each layer is carefully chosen to balance the task's complexity and the dataset size, ensuring enough model expressiveness while minimizing the risk of overfitting. To solve the nonlinear relationship between the gravity anomaly data and the sea depth, the ReLU activation function is used for the hidden layer, and the gradient vanishing problem is also reduced, and the formula is as follows:

$$f(x) = \max(0, x) \tag{5}$$

The Adam optimizer is selected to optimize the personalized learning rate of each parameter by combining the momentum and adaptive learning rate adjustment mechanism, and the parameter update strategy is more efficient and robust. The initial learning rate is set to 0.001, the number of training iterations is set to 40, and the batch size is set to 512. To prevent overfitting, we implemented early stopping and learning rate decay as callback functions. Specifically, training is halted if the validation loss fails to improve for 10 consecutive epochs. When the monitored indicator (root mean square error) did not improve significantly for three consecutive rounds, the learning rate was halved. The minimum improvement threshold was set to 0.001, and the minimum learning rate was 1×10^{-6}, which helped the model achieve better convergence during the later stages of training.

The training process proceeds as follows: the training dataset is fed into the Fully Connected Deep Neural Network (FCDNN), which generates prediction outputs. The loss value, representing the difference between the predicted outputs and the actual training data, is then calculated. If the loss value continues to decrease and the maximum number of iterations has not been reached, the network's biases and weights are adjusted using the Adam optimization algorithm. This iterative process is repeated until the loss value stabilizes, marking the completion of the neural network training.

During this process, the order of the prediction outputs is maintained consistently with the data order from the training phase to ensure the accuracy of the model's predictions. Subsequently, using the grid structure of the GEBCO model, the calculated long-wavelength and short-wavelength gravity anomalies, along with their residuals, are interpolated to a $1' \times 1'$ grid using the bicubic interpolation method. Specifically, the weighted average of the sixteen nearest sampling points to each grid node is calculated to generate the feature data for those nodes. These interpolated features are then fed into the FCDNN model as the prediction dataset, and the seabed topography model of the South China Sea, termed FCD_Depth_SCS, is constructed based on the predicted seafloor depths at these grid nodes. To validate the accuracy of the FCD_Depth_SCS model, comparative analyses were performed with existing submarine topography models, providing a comprehensive evaluation of its performance and precision.

4. Result and Analysis

4.1. Seabed Topography Model of the South China Sea

The FCD_Depth_SCS model, developed using the FCDNN neural network for the study area, is illustrated in Figure 5. The figure reveals that the waters surrounding the Paracel Islands are the shallowest, while the trenches along the eastern margin of the South China Sea represent the deepest regions.

4.2. Comparison with Shipborne Bathymetric Data

To evaluate the accuracy of the FCD_Depth_SCS model, a seabed topography model of the South China Sea was generated using the gravity geology method (GGM) and named the GGM_Depth model. Additionally, the GEBCO_2024, SIOv25.1, and DTU18 models were incorporated for comparison. The FCD_Depth_SCS, GGM_Depth, GEBCO_2024, SIOv25.1, and DTU18 models were interpolated to the checkpoint locations using bicubic interpolation and compared with the bathymetric data at these checkpoints. Standard deviation (STD), root mean square error (RMS), and mean absolute percentage error (MAPE/%) were used as evaluation metrics.

Mean Absolute Percentage Error (MAPE/%) is a commonly used metric for evaluating predictive accuracy, measuring the percentage difference between predicted and actual values [19,20,25,34]. Its primary advantage is that it expresses the relative error as a

percentage, enhancing comparability across prediction problems with different scales and providing a clear measure of relative error magnitude. The calculation formula is as follows:

$$\text{MAPE} = \frac{100\%}{n}\sum_{i=1}^{n}\left|\frac{\hat{y}_i - y_i}{y_i}\right| \tag{6}$$

In the above formula, $\hat{y}_i$ represents the i-th predicted sea depth value, y_i denotes the i-th measured water depth value, and n is the total number of checkpoints.

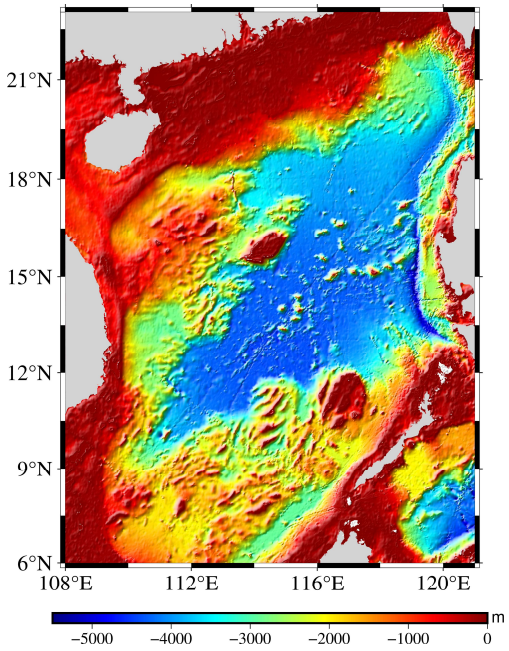


Figure 5. Seabed topography model of the South China Sea (FCD_Depth_SCS model).

Table 1 presents the statistical results comparing the bathymetric predictions of five models—FCD_Depth_SCS, GGM_Depth, GEBCO_2024, SIOv25.1, and DTU18—against the shipborne bathymetric values at the verification points. As shown in Table 1, the FCD_Depth_SCS model achieved a standard deviation (STD) of 44.755 m relative to the shipborne bathymetric values, which is significantly lower than the STDs of GGM_Depth (58.874 m), GEBCO_2024 (82.234 m), SIOv25.1 (108.241 m), and DTU18 (189.670 m). The MAPE of the FCD_Depth_SCS model was 2.903%, demonstrating higher predictive accuracy compared to GGM_Depth (3.663%), GEBCO_2024 (3.733%), SIOv25.1 (5.149%), and DTU18 (9.095%). The lower STD and MAPE values of the FCD_Depth_SCS model indicate reduced prediction dispersion and higher accuracy, which can be attributed to the model's ability to effectively fuse gravity anomaly data through the FCDNN neural network. This highlights the advantage of using a deep learning approach to model the nonlinear relationships between gravity anomalies and bathymetry, enabling more precise topographic predictions.

The results also emphasize the limitations of traditional and global models like GGM, GEBCO_2024, SIOv25.1, and DTU18 in capturing fine-scale regional variations, particularly in complex areas like the South China Sea. These models often prioritize global consistency over regional precision, which may explain their higher STDs and MAPEs. In contrast, the FCD_Depth_SCS model leverages the strengths of gravity anomaly data and deep learning to produce a more localized and accurate representation of seabed topography. This demonstrates the effectiveness and practicality of the proposed method for high-resolution bathymetric modeling.

Table 1. Statistical results comparing the FCD_Depth_SCS, GGM_Depth, GEBCO_2024, SIOv25.1, and DTU18 models with shipborne depth measurements at check points (Unit: m).

Model	Max	Min	Mean	STD	RMS	MAPE/%
FCD_Depth_SCS	1245.725	−857.709	0.187	44.755	44.756	2.903
GGM_Depth	1133.773	−1524.209	0.321	58.874	58.875	3.663
GEBCO_2024	842.874	−842.579	2.181	82.234	82.263	3.733
SIOv25.1	2137.575	−1964.993	6.786	108.241	108.454	5.149
DTU18	2130.733	−2762.660	31.904	186.967	189.670	9.095

Figure 6 presents the difference histogram and scatter plot comparing the five models to shipborne bathymetry. The histogram (top) indicates that the differences for all five models are centered around zero and follow a normal distribution. Notably, the differences for the FCD_Depth_SCS model are the most concentrated and symmetrical, demonstrating high prediction accuracy for sea depth. In contrast, the differences for the GGM_Depth, GEBCO_2024, SIOv25.1, and DTU18 models are more dispersed, with the DTU18 model showing the widest error range and lowest accuracy. The scatter plot (bottom) further illustrates that the FCD_Depth_SCS model maintains relatively stable errors across different water depths. In comparison, other models, particularly SIOv25.1 and DTU18, exhibit significant error fluctuations at greater depths, highlighting the FCD_Depth_SCS model's superiority in deepwater predictions.

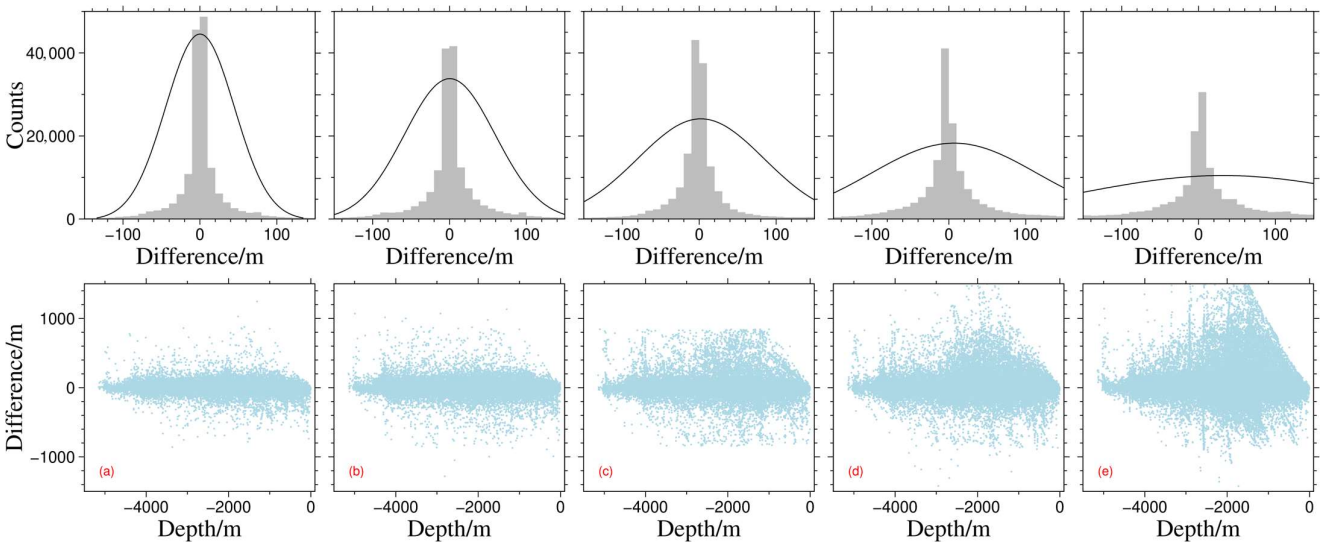


Figure 6. Difference histograms and scatter plots comparing the FCD_Depth_SCS, GGM_Depth, GEBCO_2024, SIOv25.1, and DTU18 models with shipborne depth measurements at checkpoints: (**a**) FCD_Depth_SCS, (**b**) GGM _Depth, (**c**) GEBCO_2024, (**d**) SIOv25.1, (**e**) DTU18.

Figure 7 illustrates the spatial distribution of the differences between the predictions of the five models and the shipborne depth measurements at the checkpoints. The distribution of prediction errors across the South China Sea varies among the models. The FCD_Depth_SCS model demonstrates a narrow error range and high spatial uniformity, while the error distributions of the other models are less consistent, particularly in specific regions. As shown in Figure 7a, most of the FCD_Depth_SCS model's error values are concentrated between −150 m and 150 m, with a relatively uniform spatial distribution and no significant areas of large errors, indicating higher prediction accuracy. In contrast, the error distribution of the GGM_Depth model in Figure 7b is more scattered, with notably larger errors in certain areas, particularly in the northern and central regions of the South China Sea, showing a degree of spatial non-uniformity. The GEBCO_2024 model, depicted

in Figure 7c, exhibits substantial errors in the central and southern regions, especially in deep-sea areas. The SIOv25.1 model in Figure 7d shows significant error fluctuations throughout the South China Sea, with pronounced errors in the central and southern regions. The DTU18 model, shown in Figure 7e, has the largest error range, particularly in the southern and central regions, indicating lower prediction accuracy. Overall, the FCD_Depth_SCS model demonstrates the smallest and most evenly distributed prediction errors across the entire South China Sea, reflecting its superior accuracy and stability. In contrast, the other models exhibit greater error fluctuations in specific regions, particularly the DTU18 and SIOv25.1 models, which show large and uneven error distributions.

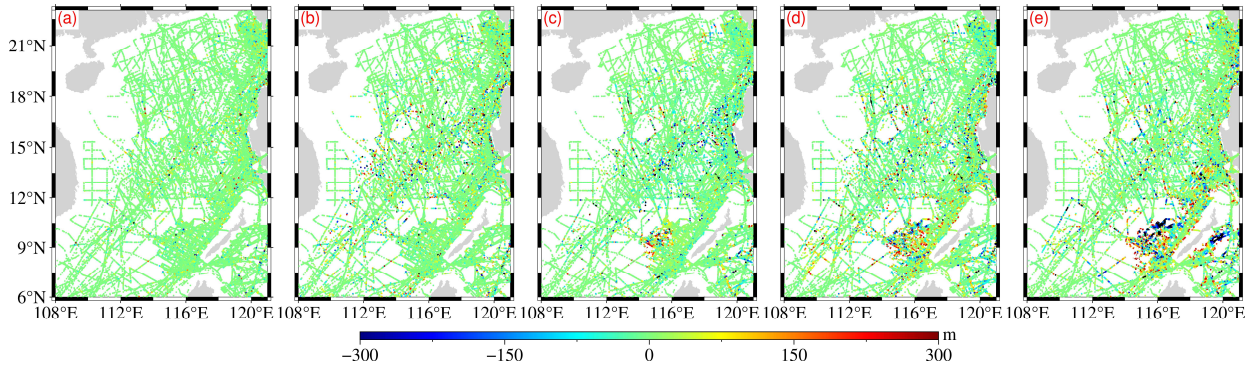


Figure 7. Spatial distribution of depth differences between FCD_Depth_SCS, GGM_Depth, GEBCO_2024, SIOv25.1, and DTU18 models and shipborne depth measurements at check points: (**a**) FCD_Depth_SCS, (**b**) GGM _Depth, (**c**) GEBCO_2024, (**d**) SIOv25.1, (**e**) DTU18.

4.3. Comparative Analysis of Inversion Results Across Different Water Depths and Distances from Shore

To evaluate the accuracy of the five models at varying distances from the coastline, the differences between the predicted and shipborne bathymetric values were analyzed based on the verification points' distances from the coast. The results are summarized in Table 2. As shown in Table 2, the FCD_Depth_SCS model consistently outperforms the other models in all distance intervals (>0 km, >10 km, >20 km, >30 km, >40 km). Across all distance ranges, the RMS and STD values of the FCD_Depth_SCS model remain the lowest, ranging from 44.755 m to 46.836 m, indicating minimal deviations between the model's predictions and the shipborne measurements. In contrast, the errors of the GGM_Depth, GEBCO_2024, SIOv25.1, and DTU18 models exhibit significant fluctuations. Furthermore, the MAPE of the FCD_Depth_SCS model is substantially lower than that of the other models and decreases with increasing distance from the coastline. Notably, at distances >40 km, the MAPE of the FCD_Depth_SCS model is only 1.503%, demonstrating minimal deviation from shipborne measurements and indicating that the model's accuracy improves with increasing distance from shore.

Table 3 presents the statistical comparison of the five models with shipborne bathymetric data for water depths greater than and less than 500 m. As shown in Table 3, the FCD_Depth_SCS model outperforms the other models in both depth ranges. In shallow waters (less than 500 m), the FCD_Depth_SCS model achieves an RMS of 29.227 m, better than most models. In deeper waters (greater than 500 m), the RMS is 48.468 m. Additionally, the MAPE for the FCD_Depth_SCS model in deep water is only 1.512%, much lower than other models, particularly the 6.940% for the DTU18 model. Overall, the FCD_Depth_SCS model demonstrates stable and accurate bathymetric predictions, especially in deep-water areas.

Table 2. Statistical results of the comparison between each model and the shipborne depth measurements at different distances from the coastline (Unit: m).

Distance/m (Check Points Number)	Model	Max	Min	Mean	STD	RMS	MAPE/%
>0 160,476	FCD_Depth_SCS	1245.725	−857.709	0.187	44.755	44.756	2.903
	GGM_Depth	1133.773	−1524.209	0.321	58.874	58.875	3.663
	GEBCO_2024	842.874	−842.579	2.181	82.234	82.263	3.733
	SIOv25.1	2137.575	−1964.993	6.786	108.241	108.454	5.149
	DTU18	2130.733	−2762.660	31.904	189.670	189.670	9.095
>10 138,423	FCD_Depth_SCS	1245.725	−857.709	0.202	46.836	46.837	2.091
	GGM_Depth	1133.773	−1524.209	0.067	61.759	61.759	2.681
	GEBCO_2024	842.874	−842.579	1.886	86.898	86.919	3.187
	SIOv25.1	2137.575	−1964.993	7.413	114.753	114.992	4.237
	DTU18	2130.733	−2762.660	35.127	199.381	202.452	8.245
>20 128,024	FCD_Depth_SCS	1028.779	−857.709	0.266	46.370	46.371	1.776
	GGM_Depth	1071.129	−1524.209	0.148	60.973	60.974	2.336
	GEBCO_2024	842.874	−842.579	1.685	87.897	87.913	2.994
	SIOv25.1	2137.575	−1964.993	8.039	115.665	115.944	3.906
	DTU18	2130.733	−2762.660	35.269	202.316	205.367	7.858
>30 117,243	FCD_Depth_SCS	1028.779	−857.709	−0.074	46.561	46.561	1.612
	GGM_Depth	1071.129	−1524.209	−0.324	61.477	61.477	2.130
	GEBCO_2024	842.874	−842.579	1.565	87.867	87.881	2.739
	SIOv25.1	1861.754	−1964.993	7.886	114.788	115.059	3.622
	DTU18	2130.733	−2762.660	31.350	200.319	202.757	6.954
>40 108,386	FCD_Depth_SCS	860.553	−857.709	−0.110	44.969	44.969	1.503
	GGM_Depth	1071.129	−1524.209	−0.326	60.624	60.625	1.981
	GEBCO_2024	842.874	−842.579	0.351	84.595	84.596	2.356
	SIOv25.1	1861.754	−1964.993	6.403	114.295	114.474	3.374
	DTU18	2130.733	−2762.660	25.710	196.118	197.796	6.167

Table 3. Statistical results comparing each model with shipborne depth measurements in the ranges of water depth greater than 500 m and less than 500 m (Unit: m).

Depth/m (Check Points Number)	Model	Max	Min	Mean	STD	RMS	MAPE/%
≤500 37,150	FCD_Depth_SCS	227.209	−737.291	−1.639	29.181	29.227	7.523
	GGM_Depth	354.972	−992.283	−0.979	34.392	34.406	9.379
	GEBCO_2024	595.464	−809.511	0.086	41.006	41.006	8.077
	SIOv25.1	594.921	−869.450	−1.584	47.092	47.119	10.713
	DTU18	581.641	−824.270	9.480	56.532	57.321	16.249
>500 123,326	FCD_Depth_SCS	1245.725	−857.709	0.737	48.463	48.468	1.512
	GGM_Depth	1133.773	−1524.209	0.712	64.446	64.450	1.941
	GEBCO_2024	842.874	−842.579	2.811	91.056	91.100	2.425
	SIOv25.1	2137.575	−1964.993	9.308	120.624	120.982	3.473
	DTU18	2130.733	−2762.660	38.659	210.540	214.060	6.940

4.4. Inversion Results in Different Sea Areas

To delve deeper into the relationship between the accuracy of seabed topography models derived from neural network inversion and both sea area size and seabed terrain complexity, experiments were conducted in the South China Sea. These experiments utilized four sea areas that differed in size and topographic complexity. This analysis

aims to provide a theoretical foundation for the future development of a global seabed topography model.

Figure 8A shows the sea depth and distribution of the four selected areas. Area A (8°N–10°N, 109°E–112°E) is in the southwestern part of the South China Sea. This region features an open sea surface, deep waters, and relatively flat terrain, with an average sea depth of −1848.6 m. Area B (13°N–15°N, 113°E–115°E), situated in the central South China Sea, is the smallest of the four regions and has the deepest average sea depth of −3915.9 m, with a maximum depth of −4570.0 m. The area includes both flat seabeds and complex topographic structures, particularly near an offshore seamount to the north. It exhibits relatively minor topographic variations, as indicated by the smallest standard deviation of sea depth among the four regions. Area C (19°N–21°N, 114°E–117°E) lies near the northern coastal region of the South China Sea and is characterized by shallow waters, with an average depth of approximately −1207.8 m and relatively gentle seabed topography. In contrast, Area D (12°N–15°N, 118°E–120°E), located in the eastern part of the South China Sea, has the most complex and varied seabed terrain, with a maximum depth of −5150.0 m and a minimum depth of −22.5 m. The average depth is −2620.8 m, and the standard deviation of sea depth is as high as 1186.5 m, reflecting significant topographic undulations. This area includes diverse features such as seamounts and deep-sea basins, making it the most topographically diverse region among the four.

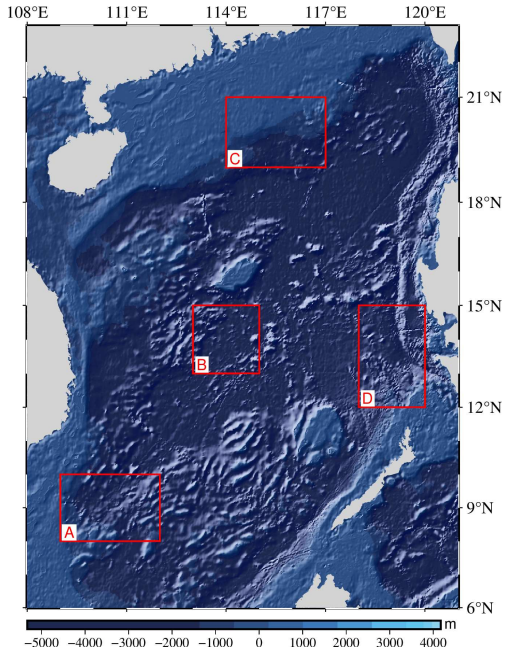


Figure 8. Map of the distribution of different regions, where the letters A, B, C, and D represent the selected distinct regions.

Table 4 presents the statistical results of the inversion for the four sea areas (A, B, C, and D) using the FCDNN neural network, compared with shipborne bathymetric data. It also includes a comparison of the FCD_Depth_SCS model with shipborne bathymetry in each area. As shown in Table 4, the FCD_Depth_SCS model, when applied without regional partitioning, performs better in regions A, B, and C, particularly in regions A and C, where the terrain is relatively flat or exhibits minimal variation. In these areas, the RMS and MAPE of the non-partitioned model are significantly lower than those of the partitioned model. For example, in region C, the RMS and MAPE for the non-partitioned model are 10.864 m and 0.552%, respectively, whereas for the partitioned model, they are

18.714 m and 1.854%, respectively. This suggests that regions with simpler terrain are better suited for non-partitioned inversion, as it can more effectively capture terrain features.

Table 4. Statistical results comparing the depth inversion results of different regions with shipborne depth measurements (Unit: m).

Region Ship Survey Points Number	Model	Max	Min	Mean	STD	RMS	MAPE/%
A 4740	FCD_Depth_SCS_A FCD_Depth_SCS	277.899 293.955	−243.438 −162.899	0.313 −0.768	37.991 24.996	37.992 25.008	1.690 0.903
B 11,533	FCD_Depth_SCS_B FCD_Depth_SCS	203.534 391.481	−266.417 −282.010	0.674 1.539	35.020 34.305	35.026 34.339	0.591 0.500
C 7941	FCD_Depth_SCS_C FCD_Depth_SCS	123.384 89.309	−115.254 −77.286	0.277 −0.236	18.714 10.864	18.716 10.866	1.854 0.552
D 39,432	FCD_Depth_SCS_D FCD_Depth_SCS	1430.265 1745.522	−2283.158 −2055.073	1.147 −6.024	98.529 162.879	98.536 162.990	2.008 2.345

In contrast, in region B, despite its relatively complex terrain, the non-partitioned model performs slightly better than the partitioned model, achieving higher accuracy overall. However, in region D, which has the most complex terrain of the four areas, the partitioned model significantly outperforms the non-partitioned model. The RMS and MAPE of the partitioned model are 98.529 m and 2.008%, respectively, which are notably lower than the RMS (162.879 m) and MAPE (2.345%) of the non-partitioned FCD_Depth_SCS model. This demonstrates that the partitioned model is more effective at capturing subtle terrain variations and achieving higher accuracy in areas with complex topography.

The above results indicate a close link between inversion accuracy and regional terrain complexity. The size of the region has minimal impact on inversion accuracy. For areas with flat or simple terrain, the non-regional model is more appropriate. In contrast, for regions with complex terrain, the partitioned model is better suited to enhance inversion accuracy.

To further validate the external accuracy of the proposed neural network approach, an additional region, region E, located outside the primary study area, was introduced. As shown in Figure 9, region E spans a latitude range of 20°N to 23°N and a longitude range of 122°E to 125°E. Using the FCDNN neural network, combined with shipborne bathymetric data and gravity anomaly data, the seabed topography for region E was modeled. The data processing workflow for this additional validation is illustrated in Figure 4.

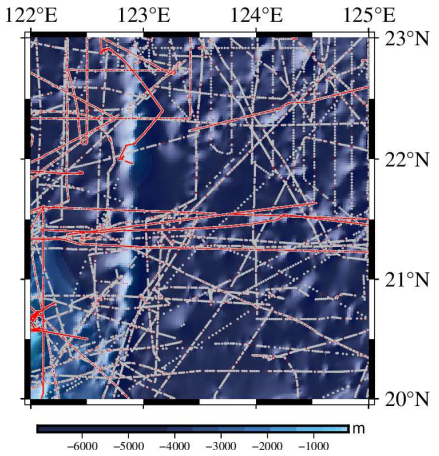


Figure 9. Geographical location of region E for external accuracy validation.

Table 5 demonstrates that the FCD_Depth_SCS_E model achieves highly stable inversion results, with an STD of 37.839 m and a MAPE of 1.018%. While the RMS is slightly higher than that of the GEBCO_2024 model (44.379 m), the FCD_Depth_SCS_E model significantly outperforms the other models, including GGM_Depth, SIOv25.1, and DTU18, across all metrics. These results highlight the effectiveness of the FCDNN neural network in accurately inverting seabed depths and its robustness in handling external validation areas.

Table 5. Statistical results of the inversion results of region E and the comparison of other models with the bathymetric values of the ship (unit: m).

Model	Max	Min	Mean	STD	RMS	MAPE/%
FCD_Depth_SCS_E	422.116	−375.943	5.343	37.839	38.214	1.018
GGM_Depth	546.732	−591.974	19.816	59.492	62.705	2.516
GEBCO_2024	412.109	−413.319	−0.645	44.374	44.379	1.182
SIOv25.1	539.314	−2062.785	6.666	75.611	75.904	2.258
DTU18	2190.129	−2308.001	46.320	181.105	186.934	6.640

5. Conclusions

In this paper, the FCDNN neural network was used to integrate gravity anomaly data and ship bathymetry data to construct a seabed topography model for the South China Sea (108°E–121°E, 6°N–23°N) with a grid resolution of $1' \times 1'$, termed the FCD_Depth_SCS model. The accuracy of the FCD_Depth_SCS model was comprehensively evaluated, and the following conclusions were drawn:

The FCD_Depth_SCS model demonstrated superior accuracy, achieving an STD of 44.755 m and a MAPE of 2.903%, significantly outperforming the GGM_Depth, GEBCO_2024, SIOv25.1, and DTU18 models, which had STDs of 58.874–189.670 m and MAPEs of 3.663–9.095%. The higher errors in these models stem from their limitations: GGM_Depth relies on simplified assumptions like constant density contrast, while global models such as GEBCO_2024 and DTU18 prioritize large-scale consistency over regional precision. In contrast, the FCD_Depth_SCS model integrates gravity anomaly data with the FCDNN neural network, capturing complex regional features with greater accuracy.

When compared with the measured sea depth values at verification points in different water depth ranges and distances from the shore, the results show that the FCD_Depth_SCS model is particularly stable in deep-water predictions. In contrast, other models, such as SIOv25.1 and DTU18, show significant error fluctuations at larger water depths. The FCD_Depth_SCS model also performs better in offshore areas, with accuracy gradually decreasing as the distance from the coastline reduces. This suggests that the FCD_Depth_SCS model outperforms other models in both prediction accuracy and stability.

Four different sea areas (A, B, C, D) of varying sizes were selected in the South China Sea to analyze the relationship between model accuracy, area size, and topography. The results showed that the non-partitioned model performed significantly better in regions A and C, where the terrain is relatively flat or exhibits minimal variation. In these areas, the STD and MAPE of the non-partitioned model were lower than those of the partitioned model. In region B, despite the complex terrain, the non-regional model still slightly outperformed the partitioned model. However, in region D, which has the most complex terrain, the partitioned model performed better, with an STD of 98.529 m and a MAPE of 2.008%, compared to the non-partitioned model's STD of 163.879 m and MAPE of 2.345%. This indicates that the partitioned model is more effective at capturing topographic changes and provides higher accuracy in regions with complex terrain.

Overall, the inversion accuracy is primarily influenced by terrain complexity, with area size having minimal impact. The non-partitioned model is more suitable for flat areas, while partitioning is necessary to improve accuracy in regions with complex terrain.

Author Contributions: Conceptualization, J.Y.; Data curation, C.Y.; Formal analysis, D.D. and J.G.; Investigation, J.Y.; Methodology, J.Y. and C.Y.; Supervision, J.G., D.A. and D.Y.; Validation, C.Y.; Visualization, D.D.; Writing—original draft, C.Y.; Writing—review and editing, D.D., J.G., D.A. and D.Y. All authors have read and agreed to the published version of the manuscript.

Funding: This study was supported by the Open Fund of the Key Laboratory of Marine Environmental Survey Technology and Application, Ministry of Natural Resources, P.R. China (grant no.: MESTA-2022-B002), and the Scientific Research Foundation for High-level Talents of Anhui University of Science and Technology (grant no.: 2022yjrc66).

Data Availability Statement: The data used in this study can be obtained from the corresponding author upon reasonable request.

Acknowledgments: We would like to thank the organizations that provided the gravity anomaly data, seabed topography model data, and ship bathymetry data.

Conflicts of Interest: The authors declare no conflicts of interest.

References

1. Liu, B.; Huang, J.Y.; Jiang, W.B.; Wang, W.W.; Yang, L. Seismic monitoring of sub-seafloor fluid processes in the Haima cold seep area using an Ocean Bottom Seismometer (OBS). *Earth Planet. Phys.* **2023**, *7*, 582–602. [CrossRef]
2. Wan, X.Y.; Annan, R.F.; Wang, W.B. Assessment of HY-2A GM data by deriving the gravity field and bathymetry over the Gulf of Guinea. *Earth Planets Space* **2020**, *72*, 151. [CrossRef]
3. Hu, M.; Zhang, S.; Jin, T.; Wen, H.; Chu, Y.; Jiang, W.; Li, J. A new generation of global bathymetry model BAT_WHU2020. *Acta Geod. Cartogr. Sin.* **2020**, *49*, 939–954.
4. Sun, Y.; Zheng, W.; Li, Z.; Zhou, Z. Improved the Accuracy of Seafloor Topography from Altimetry-Derived Gravity by the Topography Constraint Factor Weight Optimization Method. *Remote Sens.* **2021**, *13*, 2277. [CrossRef]
5. Sun, H.; Li, Q.; Bao, L.; Wu, Z.; Wu, L. Progress and Development Trend of Global Refined Seafloor Topography Modeling. *Geomat. Inf. Sci. Wuhan Univ.* **2022**, *47*, 1555–1567.
6. Xiang, X.S.; Wan, X.Y.; Zhang, R.; Li, Y.; Sui, X.H.; Wang, W.B. Bathymetry Inversion with the Gravity-Geologic Method: A Study of Long-Wavelength Gravity Modeling Based on Adaptive Mesh. *Mar. Geod.* **2017**, *40*, 329–340. [CrossRef]
7. Xing, J.; Chen, X.-X.; Ma, L. Bathymetry inversion using the modified gravitygeologic method:application of the rectangular prism model and Tikhonov regularization. *Appl. Geophys.* **2020**, *17*, 377–389. [CrossRef]
8. Zhu, F.S.; Guo, J.Y.; Zhang, H.Y.; Huang, L.Y.; Sun, H.P.; Liu, X. SDUST2020MGCR: A global marine gravity change rate model determined from multi-satellite altimeter data. *Earth Syst. Sci. Data* **2024**, *16*, 2281–2296. [CrossRef]
9. Ibrahim, A.; Hinze, W.J. Mapping Buried Bedrock Topography with Gravity. *Groundwater* **1972**, *10*, 18–23. [CrossRef]
10. Hsiao, Y.-S.; Kim, J.W.; Kim, K.B.; Lee, B.Y.; Hwang, C. Bathymetry Estimation Using the Gravity-Geologic Method: An Investigation of Density Contrast Predicted by the Downward Continuation Method. *Terr. Atmos. Ocean. Sci.* **2011**, *22*, 347–358. [CrossRef]
11. An, D.; Guo, J.; Chang, X.; Wang, Z.; Jia, Y.; Liu, X.; Bondur, V.; Sun, H. High-precision $1' \times 1'$ bathymetric model of Philippine Sea inversed from marine gravity anomalies. *Geosci. Model Dev.* **2024**, *17*, 2039–2052. [CrossRef]
12. Chen, W.; Hu, M.; Zhang, J.; Lin, J.; Zhang, B. Gravity admittance analysis and its implications for the formation of the Tamu Massif in the west Pacific Ocean. *Period. Ocean. Univ. China* **2023**, *53*, 94–103.
13. Sandwell, D.T.; Smith, W.H.F. Global seafloor topography from dense satellite altimetry and sparse ship soundings (MGE). *Third ERS Symp. Space Serv. Our Environ.* **1997**, *277*, 1956–1962.
14. Fan, D.; Li, S.S.; Li, X.X.; Yang, J.J.; Wan, X.Y. Seafloor Topography Estimation from Gravity Anomaly and Vertical Gravity Gradient Using Nonlinear Iterative Least Square Method. *Remote Sens.* **2020**, *13*, 64. [CrossRef]
15. Ouyang, M. Research progress and prospects of seabed topography inversion from altimetry data. *Prog. Geophys.* **2022**, *37*, 2291–2300. (In Chinese)
16. Jiang, T.; Jiang, X.; Guo, J.; Zhang, Z. Reviewon Research Progress of Recovering Bathymetry from Satellite Altimetry Derived Data. *J. Jilin Univ. (Earth Sci. Ed.)* **2023**, *53*, 2029–2044.

17. Fan, D.; Li, S.; Ouyang, Y.; Meng, S.; Chen, C.; Xing, Z.; Zhang, C. Seafloor topography inversion using least square collocation considering nonlinear term. *Acta Geod. Et Cartogr. Sin.* **2021**, *50*, 953–971.
18. Sagawa, T.; Yamashita, Y.; Okumura, T.; Yamanokuchi, T. Satellite Derived Bathymetry Using Machine Learning and Multi-Temporal Satellite Images. *Remote Sens.* **2019**, *11*, 1155. [CrossRef]
19. Zhou, S.; Liu, X.; Sun, Y.; Chang, X.T.; Jia, Y.J.; Guo, J.Y.; Sun, H.P. Predicting bathymetry using multisource differential marine geodetic data with multilayer perceptron neural network. *Int. J. Digit. Earth* **2024**, *17*, 2393255. [CrossRef]
20. Yang, L.; Liu, M.; Liu, N.; Guo, J.Y.; Lin, L.; Zhang, Y.Y.; Du, X.; Xu, Y.S.; Zhu, C.C.; Wang, Y.K. Recovering Bathymetry from Satellite Altimetry-Derived Gravity by Fully Connected Deep Neural Network. *IEEE Geosci. Remote Sens. Lett.* **2023**, *20*, 1–5. [CrossRef]
21. Zhao, L.; Lu, S.; Qi, D.; Xu, D.; Ying, S. Daily maximum air temperature forecast based on fully connected neural network. *J. Appl. Meteorol. Sci.* **2022**, *33*, 257–269.
22. Pu, Y.; Jiang, Y.; Tian, C.; Yu, Y. Online learning behavior classification and discrimination based on fully connected neural network. *Mod. Electron. Tech.* **2023**, *46*, 89–94.
23. Liao, C.; Pang, C.; Jiang, Y.; Wu, T. Six-Component Seismic Waves Polarization Vectors Identification Based on Multi-Layer Fully Connected Neural Network. *J. Geod. Geodyn.* **2024**, *44*, 331–335+435.
24. Lumban-Gaol, Y.A.; Ohori, K.A.; Peters, R.Y. Satellite-Derived Bathymetry Using Convolutional Neural Networks and Multispectral Sentinel-2 Images. *Int. Arch. Photogramm. Remote Sens. Spatial Inf. Sci.* **2021**, *XLIII-B3-2021*, 201–207. [CrossRef]
25. Zhou, S.; Liu, X.; Guo, J.Y.; Jin, X.; Yang, L.; Sun, Y.; Sun, H.P. Bathymetry of the Gulf of Mexico Predicted with Multilayer Perceptron from Multisource Marine Geodetic Data. *IEEE Trans. Geosci. Remote Sens.* **2023**, *61*, 4208911. [CrossRef]
26. Zhu, C.C.; Yang, L.; Bian, H.W.; Li, H.P.; Guo, J.Y.; Liu, N.; Lin, L. Recovering Gravity from Satellite Altimetry Data Using Deep Learning Network. *IEEE Trans. Geosci. Remote Sens.* **2023**, *61*, 5911311. [CrossRef]
27. Wang, H.; Wan, X.; Annan, R.F. Seafloor topography prediction in the South China Sea based on convolutional neural network. *J. Geod. Geodyn.* **2024**, *44*, 287–292.
28. Harper, H.; Sandwell, D.T. Global Predicted Bathymetry Using Neural Networks. *Earth Space Sci.* **2024**, *11*, e2023EA003199. [CrossRef]
29. Guo, J.; Zhang, H.; Li, Z.; Zhu, C.; Liu, X.; Luo, H. Joint Reprocessing of Shipborne Gravity Anomalies Based on Multi-Sources: A Case Study of the Gulf of Mexico. *Geomat. Inf. Sci. Wuhan Univ.* **2023**, *48*, 1–23. (In Chinese)
30. Hao, R.J.; Wan, X.Y.; Annan, R.F. Enhanced Short-Wavelength Marine Gravity Anomaly Using Depth Data. *IEEE Trans. Geosci. Remote Sens.* **2023**, *61*, 5903109. [CrossRef]
31. An, D.C.; Guo, J.Y.; Li, Z.; Ji, B.; Liu, X.; Chang, X.T. Improved Gravity-Geologic Method Reliably Removing the Long-Wavelength Gravity Effect of Regional Seafloor Topography: A Case of Bathymetric Prediction in the South China Sea. *IEEE Trans. Geosci. Remote Sens.* **2022**, *60*, 4211912. [CrossRef]
32. Amante, C.; Eakins, B.W. ETOPO1 Arc-Minute Global Relief Model: Procedures, Data Sources and Analysis. *Psychologist* **2009**, *16*, 20–25.
33. Smith, W.H.F. On the accuracy of digital bathymetric data. *J. Geophys. Res.-Solid Earth* **1993**, *98*, 9591–9603. [CrossRef]
34. Zhou, S.; Liu, X.; Li, Z.; Zhu, C.; Yuan, J.; Guo, J.; Sun, H. 2024. Multi-layer perceptron inversion of seafloor topography in the South China Sea using multi-source marine geodetic data. *Chin. J. Geophys.* **2024**, *67*, 1368–1382. (In Chinese)
35. Hsiao, Y.-S.; Hwang, C.; Cheng, Y.-S.; Chen, L.-C.; Hsu, H.-J.; Tsai, J.-H.; Liu, C.-L.; Wang, C.-C.; Liu, Y.-C.; Kao, Y.-C. High-resolution depth and coastline over major atolls of South China Sea from satellite altimetry and imagery. *Remote Sens. Environ.* **2016**, *176*, 69–83. [CrossRef]
36. Sun, H.Y.; Feng, Y.K.; Fu, Y.G.; Sun, W.K.; Peng, C.; Zhou, X.H.; Zhou, D.X. Bathymetric Prediction Using Multisource Gravity Data Derived from a Parallel Linked BP Neural Network. *J. Geophys. Res.-Solid Earth* **2022**, *127*, e2022JB024428. [CrossRef]

Disclaimer/Publisher's Note: The statements, opinions and data contained in all publications are solely those of the individual author(s) and contributor(s) and not of MDPI and/or the editor(s). MDPI and/or the editor(s) disclaim responsibility for any injury to people or property resulting from any ideas, methods, instructions or products referred to in the content.